Wireless Power Transfer

ARTICLE

Open Access

https://doi.org/10.48130/wpt-0026-0023

Wireless Power Transfer **2026**, 13: e031

Dynamic charging system with reduced power semiconductor device count

Konstantina Dimitriadou[1], Ioannis Albanopoulos[1], Nick Papanikolaou[1*] and Yongheng Yang[2]

[1] *Department of Electrical and Computer Engineering, Democritus University of Thrace, 67100 Xanthi, Greece*
[2] *College of Electrical Engineering, Zhejiang University, Hangzhou 310027, China*
* Correspondence: npapanik@ee.duth.gr (Papanikolaou N)

Abstract

This article presents a cost-effective electric vehicle (EV) dynamic wireless charging (DWC) system, which enables sufficient and continuous power transfer to the receiver without demanding an inordinate amount of semiconductor devices and passive elements, the establishment of a real-time communication link between the ground and vehicle assemblies, or the deterioration of the receiver power density. A single high-frequency inverter (HFI) along with a series reactive power compensator (SRPC) configuration is employed for the energization of multiple resonant tanks, composed of track-based magnetic couplers and series compensation capacitors, whilst the integrated AC switching (ACS) subsystem facilitates their selective activation. The SRPC incorporation contributes to the suppression of the charging power fluctuations and the accomplishment of zero-voltage switching (ZVS) transitions for the HFI power devices. Extensive finite element analysis (FEM) tests, realized on ANSYS MAXWELL, are utilized for the explicit design of proposed couplers, aiming at the minimization of the overall laying cost. Additionally, a comprehensive co-simulation study, conducted on the software packages MATLAB/Simulink and PLECS, is deployed for the obtainment of steady-state and dynamic results, which substantiate the effectiveness and smooth operation of the proposed system. Concurrently, a power loss analysis along with a PLECS thermal study is carried out for the evaluation of the dynamic EV charger performance.

Keywords: Continuous power transfer, Dynamic wireless charging (DWC), Electric vehicle (EV), Low-laying cost, Series reactive power compensator (SRPC), Track-based magnetic coupler

Citation: Dimitriadou K, Albanopoulos I, Papanikolaou N, Yang Y. 2026. Dynamic charging system with reduced power semiconductor device count. *Wireless Power Transfer* 13: e031 https://doi.org/10.48130/wpt-0026-0023

Introduction

Recently, the ever-growing public awareness regarding the environmental impact of conventional vehicles has expedited the increase of the electric vehicle (EV) penetration rates in the transportation market and the expanded development of EV charging infrastructure. In this regard, dynamic wireless charging (DWC) systems, which allow EVs to pick up energy in motion, constitute one of the most demanding, yet promising, concepts, as their deployment could be a competent solution for the restricted cruising range issue of EVs.

The main targets of the DWC system design process are adequate and continuous power delivery to the EV, as well as the minimization of the overall installation cost. Therefore, various magnetic coupler and power supply configurations have been proposed in the literature. First, segmented topologies, i.e., arrays of windings with dimensions similar to the receiver ones, have been developed, since they guarantee enhanced coupling conditions. For instance, rectangular-shaped couplers are adopted, each accompanied by an individual high-frequency inverter (HFI)[1]. Similarly, unipolar and bipolar coils are placed alternately, in order to eliminate the cross-coupling between adjacent transmitters and the ensuing output power pulsations[2]. This approach inevitably leads to the immoderate increase of the total cable length and converter modules needed for the system installation. To address this matter, the employment of sparsely laid transmitting coils and a self-adaptive two-pole receiver winding to stabilize the coupling between the ground and vehicle assemblies was proposed[3]. A repeater coil-based structure has also been deployed, where the mutual inductance formed between adjacent transmitters is utilized to supply two neighboring resonant tanks with one HFI[4]. What is more, a soft-switched HFI, capable of accommodating two transmitter windings with a reduced switch number, has been developed[5]. To further decrease the necessary power electronics components, a switchable inductively coupled connector for the selective energization of each transmitter by a common AC bus[6] and a push-pull type inverter for the interconnection of the couplers to the DC bus[7] have been employed. Additionally, the supply of the entire charging lane by one HFI and the utilization of the transmitter self-inductance change for their selective activation have been proposed[8]. Nevertheless, the consequent output power fluctuations are significant.

Evidently, even the most advantageous and cost-efficient works[5–7], do not sufficiently tackle the DWC system laying cost issues. Thus, track-based topologies, which use longer transmitting coils compared to the EV one, have been investigated. The power supply rail configurations do, in fact, benefit the mitigation of the copper usage. The drawbacks of such structures include the mandatory deployment of numerous ferrite cores, whose fragile nature could render the installation not enduring, the intense electromagnetic field emissions, and fluctuations of the induced voltage to the pickup coil. Certain works utilize multiphase EV coils to smooth out the variations at the expense of a lightweight secondary side[9,10], while others increase the transmitter winding number, thereby compromising the litz wire length minimization[11]. Moreover, complex coil layouts, which are considerably successful in suppressing the charging power fluctuations, yet not truly cost-effective, are proposed[12,13]. Finally, frequency modulation techniques are recommended for the maximization of the power delivered by each individual HFI to the corresponding tank without, however, adequately confronting the output power variations[14]. It is worth noting that,

© The Author(s)

https://doi.org/10.48130/wpt-0026-0023

except for studies according to Gomes et al.[14] and for the cases that the EV position trace is nonobligatory[8–11], the remainder of the aforementioned publications do not include a communication link-free vehicle detection method needed for the selective activation of the transmitting coils. For this purpose, the modulation of the HFI duty cycle based on its DC active power could be deployed[15,16].

In light of the above, this article presents a cost-efficient DWC system, which is composed of an array of track-based couplers, each accompanied by a series compensation capacitor. A single HFI supplies multiple transmitters, contributing to the reduction of requisite semiconductor devices. Compared to prior art[17], it is characterized by remarkably low laying cost, and it ensures the soft-switched transitions of the HFI devices. Furthermore, it guarantees sufficient attenuation of the charging power fluctuations and features an EV position detection system for the selective energization of the transmitters, whilst not requiring extra passive elements or the compromise of the receiver's compact design.

Proposed EV dynamic wireless charging system

In Fig. 1, the schematic diagram of the proposed DWC system is depicted. Specifically, the power receiver is equipped with a series-compensated resonant circuit, a diode bridge utilized for the AC secondary current rectification, and an output filtering capacitor responsible for the suppression of the charging current ripples. With respect to the primary side, a SiC (Silicon Carbide) metal oxide semiconductor field effect transistor (MOSFET)-based full bridge comprises the HFI, whilst a GaN (Gallium Nitride) FET-based, full-bridge configuration constitutes the series reactive power compensator (SRPC) topology. The former supplies the transmitter coil array, which is embedded in the roadway, whereas the latter is utilized for the regulation of the reactive power fluctuating through the primary circuit. Each resonant tank consists of a track-based transmitter winding (of 1.5 m length), employed for the laying cost reduction and the charging power stabilization, and a series compensation capacitor. Their interconnection to the AC bus is accomplished via the AC switching (ACS) subsystem based on the receiver position. In detail, there are two operation modes regarding the selective activation of the transmitters. When the mutual inductance between the EV and the given transmitter (T_x) is high, i.e., the receiver is located directly above it, only T_x is energized (sole operation mode [SOM]). In this case, the SRPC configuration acts as a virtual, inductive impedance, enabling the zero-voltage switching (ZVS) transitions of the HFI power devices. As the vehicle moves away, approaching the adjacent winding (T_{x+1}), the series connection of the two transmitters is activated (in-series operation mode [ISOM]). In this way, the continuous power transfer to the receiver is achieved, whilst the SRPC, now operating as a virtual, capacitive impedance, further facilitates the abatement of any charging power pulsations. The increase of the mutual inductance between the EV and the second transmitter leads to its sole activation. It should be noted that the number of resonant tanks fed by a single HFI, SRPC pair depends on the current handling capabilities of the two converters. In this study, a 1:1 ratio is considered (i.e., one EV is charged by a converter set). Thus, given that the average EV length is approximately equal to 5 m, whilst keeping in mind that a safety distance of 10 m needs to be retained between two EVs charging simultaneously, ten transmitters are supplied by one converter pair. The transition to the following array (T_{x11} and so on) is accomplished by an interlock mechanism, as displayed in Fig. 1.

Design process of the magnetic coupler

The track-based magnetic coupler configuration is presented in Fig. 2a. It is composed of two rectangular-shaped coils of different lengths, and its design procedure relies upon the mathematical analysis of the circuit. Particularly, the SOM manipulations are used to deduce the value of the mutual inductance between the transmitter and receiver windings ($M_{Tx\text{-}R}$), needed to achieve the desirable power transfer level (under fully aligned conditions). The results of Fig. 2b, which are derived using the simulation study parameters (Table 1), indicate that a mutual inductance of 13 μH is necessary for the delivery of 11.5 kW to the EV. Hence, the magnetic coupler characteristics are optimized so that this condition is met, whilst the minimization of the total litz wire length is also taken into account to limit the DWC system laying cost.

The two geometric parameters that influence the mutual inductance value are the length and the turn number of the two coils, while the distance between them (i.e., h) is considered fixed to 10 cm. Extensive finite element analysis (FEA) tests were performed on the software ANSYS MAXWELL to determine the magnetic coupler features. With regard to the pickup coil, its width (w_r) and length (l_r) are both set to 500 mm for simplicity and for the enhancement of the EV space utilization. Similarly, the primary

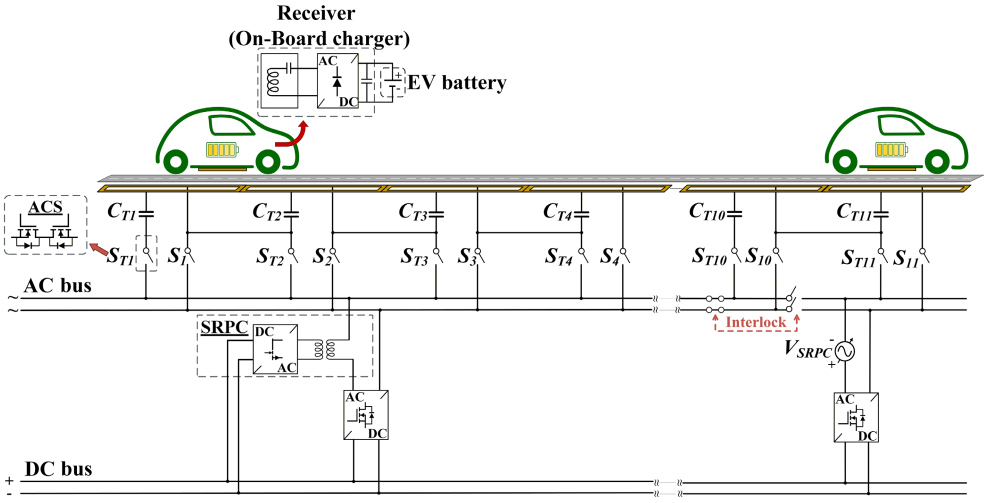


Fig. 1 Schematic diagram of the proposed dynamic wireless charging system.

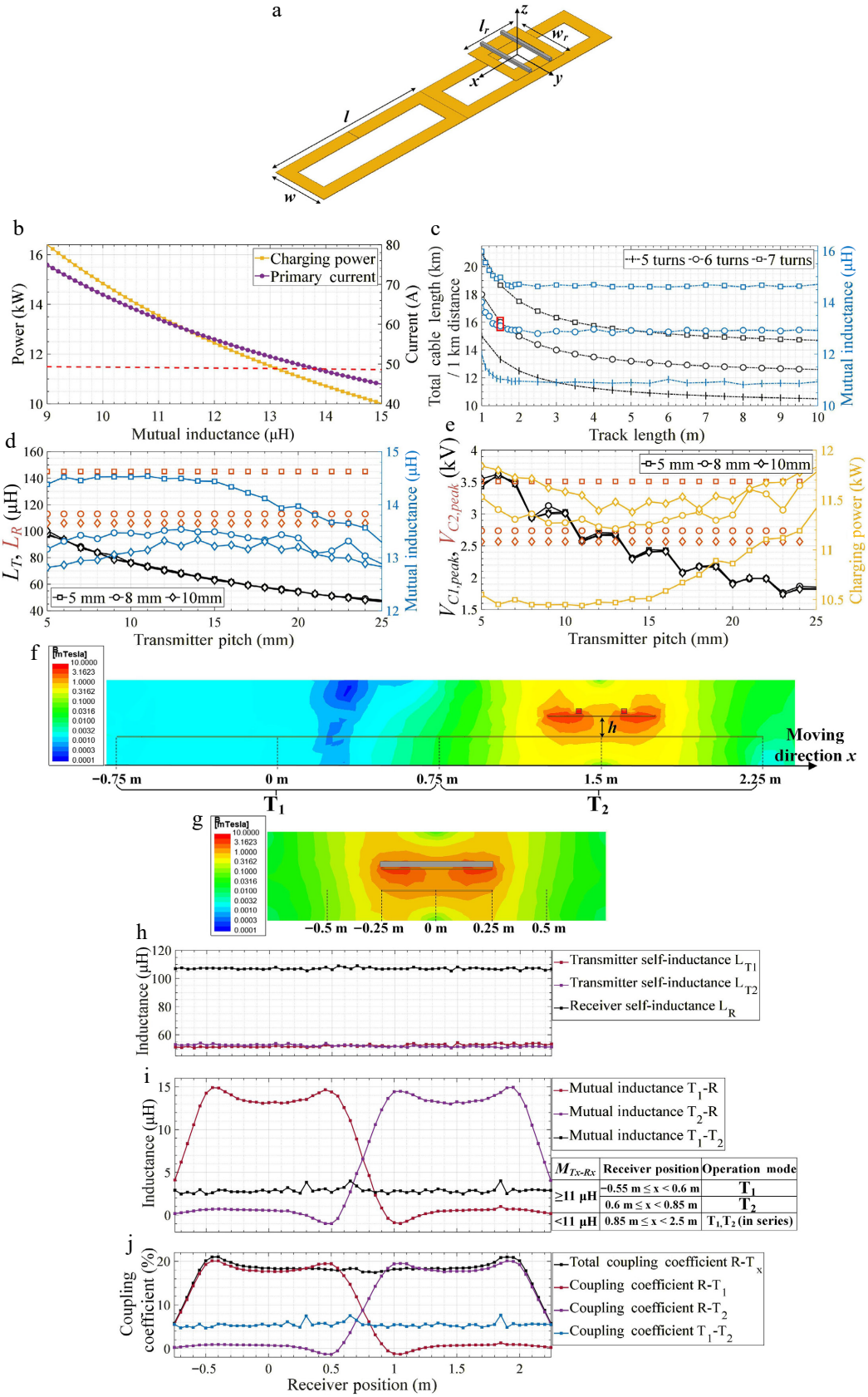


Fig. 2 Magnetic coupler design process. (a) Proposed track-based magnetic coupler (bird's-eye view). (b) Primary current and charging power vs $M_{Tx\text{-}R}$. (c) Total cable length needed per 1 km roadway distance and $M_{Tx\text{-}R}$ vs track length. (d) L_{Tx} and $M_{Tx\text{-}R}$ vs transmitter pitch for different receiver pitch values. (e) Compensation capacitor peak voltages and charging power vs transmitter pitch for different receiver pitch values. (f) B-field distribution (left side view). (g) B-field distribution (front side view). (h) Self-inductances vs EV position. (i) Mutual inductances vs EV position. (j) Coupling coefficients vs EV position.

https://doi.org/10.48130/wpt-0026-0023

winding width is kept to 500 mm, as the mirroring of this dimension facilitates the improvement of the coupling conditions. In Fig. 2c, the results for different track lengths and turn numbers are illustrated. The total litz wire length employed for the construction of a 1 km long charging roadway (C_{TOTAL}) is given by:

$$C_{TOTAL}(m) = \frac{T_{TOTAL}}{1000} C_{TRACK} = \frac{T_{TOTAL}}{1000} (l + w) 2N_T \quad (1)$$

where T_{TOTAL} is the total number of tracks, C_{TRACK} is the track wire length, N_T is the transmitter winding turn number, whilst l is its length and w is its width. Lengths larger than 10 m are not examined, since the transmitting coil resistance becomes significantly high (> 0.8 Ω). The ESRs for each presented length case are obtained using an empirical formula[18]. Litz wire of 4.5 mm diameter (675 strands, strand diameter of 0.1 mm) was utilized for the calculations. It becomes evident that the track that ensures the requisite $M_{Tx\text{-}Rx}$ value and requires the least amount of cable, i.e., 16 km, is 1.5 m long and consists of six turns, as a lower turn count results in the attenuation of the mutual inductance. Six-loop tracks of lengths larger than 3 m could further decrease the total necessary wire without resulting in any noticeable $M_{Tx\text{-}Rx}$ changes. As can be observed in Fig. 2c, $M_{Tx\text{-}Rx}$ is just slightly boosted to approximately 13.2 μH. Nevertheless, even for the shortest possible winding case (3 m), a 57% rise of the ESR (270 mΩ compared to the 155 mΩ of the preferred structure), and by extension, of the corresponding copper losses, is noted. Evidently, for higher l values, the efficiency deterioration is even worse. Furthermore, from Fig. 2c, it is discernible that the total wire needed (per 1 km roadway distance) for a 7-loop transmitting coil of length greater than 4.5 m is lower than 16 km. However, the ramped-up $M_{Tx\text{-}Rx}$ (above 14.5 μH) would lead to the reduction of the primary current root mean square (RMS) value, and hence, the charging power, as it is apparent from Fig. 2b. For the instance of a 4.5 m long track, the DC bus voltage level boost could resolve this issue; nonetheless, the wire length utilized is raised leading to the ESR (from 155 to 445 mΩ) and the associated copper losses (ΔP_{loss} = 533 W) increase. Lastly, the ferrite core placement to the transmitter array for the improvement of the coupling conditions is considered unfavorable. Their dense allocation would become imperative to avoid the fluctuations of the transmitter self-inductance value and the ensuing disruption of the resonant operation. Hence, the overall system cost would be severely affected.

With respect to the EV winding dimensions, a wire restriction of 25 m was defined. A structure that is 500 mm wide and has 12 turns complies with the cable constraint and constitutes the case with the smallest possible dimensions that allows the track elongation (beyond 1.2 m) without the mutual inductance degrading. Particularly, the w_r reduction by just 50 mm entails the retention of the transmitter length to 1.2 m, in order to achieve the desired mutual inductance value (13 μH). Consequently, the cable length required for the transmitter array construction increases from 16 km to 16.5 km (per 1 km roadway distance) compared to the selected parameter set (l = 1.5 m, w = 0.5 m). Reducing the EV winding dimensions any further results in even greater cable needs. For example, a 400 × 400 mm receiver coil limits l to 700 mm, and therefore, the total wire needed is equal to 18.85 km. It should be noted that the investigation of w_r (and thus l_r) was conducted by keeping the pitch (i.e., the distance between the centers of two adjacent turns) to a minimum, and thereby, the consequent mutual inductance value acquired for each scenario was maximized. What is more, it is worth mentioning that during the FEA study, two stacks of I102/25/25-cores (five cores per stack) were placed on top of the secondary winding for the magnetic field distribution amelioration. Their position was varied to acquire the best possible coupling conditions; the resulting distance between each core stack center and the coil center was 105 mm.

Table 1. Main system parameters/components.

	Symbol	Parameter	Value
Operational characteristics	V_{DC}	DC bus voltage level	250 V
	V_{batt}	Battery pack voltage level	400 V
	R_{Tx}	Transmitter winding ESR	155 mΩ
	R_2	Receiver winding ESR	155 mΩ
	C_{Tx}	Transmitter compensation capacitance	68 nF
	C_2	Receiver compensation capacitance	33 nF
	f_o, $f_{sw,HFI}$	Resonance frequency/ HFI switching frequency	85 kHz
	$f_{sw,SRPC}$	SRPC switching frequency	850 kHz
	C_{out}	Rectifier filtering capacitor	940 μF
Recommended components	HFI power module	CoolSiC™ MOSFET fourpack module F4-6MR20W3M1H_B11	$R_{DS,on,HFI}$ = 5.1 mΩ @ 25 °C/V_{GS} = 18 V $V_{body\ diode,HFI}$ = 2.5 V @ 25 °C/V_{GS} = −3 V $R_{body\ diode,HFI}$ = 6.25 mΩ @ 25 °C/V_{GS} = −3 V $Q_{rr,HFI}$ = 4.3 uC @ 25 °C/V_{GS} = −3 V $t_{f,HFI}$ = 33 ns @ 25 °C/V_{GS} = −3/18 V/$R_{G,off}$ = 0.51 Ω $t_{deadtime,HFI}$ = 250 ns
	SRPC power switches	CoolGaN™ Transistor G5 IGT65R025D2	$R_{DS,on,SRPC}$ = 25 mΩ @ 25 °C/V_{GS} = 6 V $V_{SD,SRPC}$ = 1.5 V @ 25 °C/V_{GS} = 0 V $R_{SD,SRPC}$ = 28.6 mΩ @ 25 °C/V_{GS} = 0 V $C_{oss,SRPC}$ = 140 pF @ V_{DS} = 250 V $E_{on,SRPC}$ =22.1 μJ @ V_{DS} = 300 V, I_D = 50.28 A $E_{off,SRPC}$ =21.2 μJ @ V_{DS} = 300 V, I_D = 50.28 A $t_{deadtime,SRPC}$ = 50 ns n_{SRPC} = 4
	ACS power module	CoolSiC™ MOSFET half bridge module FF3MR20KM1H_S	$R_{DS,on,ACS}$ = 5.2 mΩ @ 25 °C/V_{GS} = 18 V
	Rectifier diodes	SiC Shottky diode FFSH5065A	$R_{F,Rect}$ = 10 mΩ @ 25 °C $V_{F,Rect}$ = 0.8 V @ 25 °C $Q_{rr,Rect}$ = 0 nC
	Transmitter capacitor	KEMET film capacitors C4C(1)Y(2)C2330AA0(3)	C_T = 33 nF, R_{CT} = 28.3 mΩ @ 100 kHz
	Receiver capacitor	KEMET film capacitors C4C(1)Y(2)C2680AA1(3)	C_2 = 68 nF, R_{C2} = 18.3 mΩ @ 100 kHz

Subsequently, the coil pitch was refined. Fig. 2d depicts how the transmitter self-inductance and the mutual inductance $M_{Tx\text{-}R}$ are altered with the variation of the transmitter pitch p_T. Three cases of different receiver pitch p_R (i.e., 5, 8, and 10 mm) are presented. The strong correlation between the self-inductance and the pitch values should be emphasized. The p_T, and p_R increases result in the corresponding self-inductance reduction, as is visible in Fig. 2d. Therefore, the smaller p_R is, the higher the mutual inductance (for the same p_T) becomes, and as can be observed in Fig. 2e, the lower the charging power is. Simultaneously, the decrease in self-inductance leads to the mitigation of the compensation capacitor voltage stress, since the capacitance value rises for the retention of the same resonance frequency. Thus, to fulfill the application power requirements (11.5 kW), whilst maintaining the voltage stress within an acceptable range, i.e., $V_{c,peak} \leq 2.5$ kV, p_T and p_R are set to 22 mm and 10 m, respectively. This limit was set in order to abstain from the utilization of a bulky bank consisting of multiple in-series capacitors. In all, the designed magnetic coupler coils comply with the transmitter array and receiver winding cable (i.e., 16 km/1 km roadway and 25 m, accordingly), as well as the compensation capacitor voltage constraints. Concurrently, the incurred power dissipation (due to the winding ESRs) is limited.

In Fig. 2f, the B-field distribution, while the EV is moving along the two simulated transmitters, is displayed. The current excitation of the FEA study was set to 53 A, i.e., the maximum current that flows through the transmitting winding during the charging procedure. The produced field is confined, since its magnitude falls well below 31 μT on either side of the vehicle at a distance of 800 mm from the receiver coil center. The dimensions of a typical EV chassis (i.e., 1.6 × 1.6 m) and its capability to shield the passenger cabin from exposure to the electromagnetic field[19], render the movement along the transmitter array safe. Likewise, in Fig. 2g, the B-field from the front side view of the magnetic coupler is illustrated; it is significantly restricted for distances longer than 550 mm from the coil center. Additionally, in Fig. 2h, the self-inductances of each winding (L_{T1}, L_{T2}, L_R) are depicted, whereas in Fig. 2i, the mutual inductances between the primary and secondary coils, as well as the adjacent transmitters ($M_{T1\text{-}T2}$), can be observed. Notably, the self-inductances do not vary remarkably. The mutual inductance between T_1 and the receiver is practically constant and equal to 13 μH for most of the first transmitting winding length (−0.55 m ≤ x < 0.5 m). The value drops abruptly when the pickup coil approaches the following transmitter (−0.5 m ≤ x < 1 m). A similar behavior is noticed as the receiver moves along the second transmitting winding. The steep $M_{Tx\text{-}R}$ descent, recorded during the transition to the next coil, entails the inordinate primary current and charging power increase, as well as the endangerment of the transmitter equipment. Therefore, the in-series connection of the two abutting windings is imposed via the ACS subsystem during the interval when the mutual inductance between the foregoing transmitter and the receiver is lower than 11 μH. As can be seen in Fig. 2j, in this way, the coupling conditions are maintained (the equivalent coupling coefficient is the sum of the values between each transmitter and the receiver, $M_{TOT} = M_{T1\text{-}R} + M_{T2\text{-}R}$, resulting in a total mutual inductance of 13 μH), and thus, the primary current and output power fluctuations are contained. The 11 μH limit is defined so that the ISOM is not falsely activated when the EV is not perfectly aligned with the ground assembly. Any lateral displacement (along the y-axis) would lead to the $M_{Tx\text{-}Rx}$ decrease, and the ACS controller would incorrectly conclude that the vehicle is transitioning between transmitting coils, even though it is not. Consequently, the limit is set to 11 μH to take into account a lateral misalignment of ± 6 cm; an acceptable range, assuming that a speed ramp structure, forming a charging lane, is used to ease the retention of the EV in the right position.

Series reactive power compensator

The incorporation of the SRPC configuration has a twofold objective. In the SOM, it operates as a small, virtual inductor, connected in series with the HFI output, thereby imposing the ZVS conditions for its power switches. Conversely, in the ISOM, it alleviates the drastic reduction of the energy transferred to the EV ascribable to the cross-coupling between the abutting transmitters by operating as a virtual capacitance. The SRPC control scheme is based on the instantaneous power theory[20] and its diagram is depicted in Fig. 3a. The reactive power at the HFI output (Q_{HFI}) is calculated by measuring the primary current (i_1) and obtaining the fundamental harmonic component of the HFI output voltage ($v_{HFI,1}$). Concurrently, the SRPC DC current ($i_{DC,SRPC}$) is acquired, compared to a fixed, low value ($i_{ref,DC,SRPC}$), and inserted in a proportional integral (PI) controller. In this way, the DC current, and hence, the active power handled by the SRPC is minimized, i.e., the topology only participates in the reactive power exchange occurring between the primary and the secondary circuits and acts as a virtual, passive element. The result is subsequently multiplied by the control gain K, leading to $v_{ref,SPRC}$, i.e., the voltage reference value of the unipolar sinusoidal pulse width modulation (USPWM) technique utilized for the SPRC driving. The sign of the K value is modified depending on the DWC system operation mode. In the SOM, it is set to a positive value, i.e., the SRPC 'consumes' reactive power, whereas in the ISOM, K is negative, i.e., the SRPC 'generates' reactive power.

In Fig. 3b, d, the first harmonic approximation (FHA) equivalent circuit of the studied wireless EV charger in SOM and ISOM is presented, correspondingly. The mathematical analysis assumes two adjacent transmitting windings; nevertheless, the following expressions stand for the remainder of the transmitting array. Here, V_{inv} is the HFI output voltage, whilst the EV battery is emulated by a constant voltage source V_{batt}, whose reflection to the rectifier input is represented by V_{rect}. Their RMS values are given by:

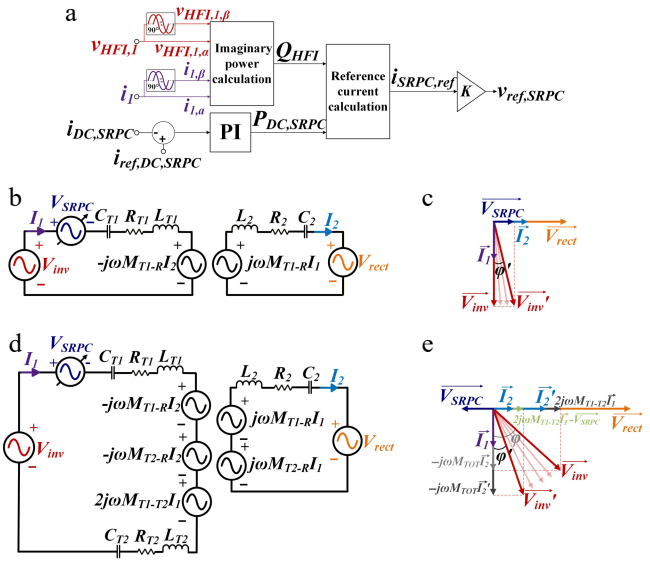


Fig. 3 SRPC operation. (a) Control diagram. (b) FHA equivalent circuit of the proposed EV DWC system in SOM. (c) SOM phasor diagram of the studied quantities. (d) FHA equivalent circuit of the proposed EV DWC system in ISOM. (e) ISOM phasor diagram of the studied quantities.

https://doi.org/10.48130/wpt-0026-0023

$$\left|\overrightarrow{Vrect}\right| = \frac{2\sqrt{2}Vbatt}{\pi},\ \left|\overrightarrow{Vinv}\right| = \frac{2\sqrt{2}V_{DC}}{\pi} \tag{2}$$

where V_{DC} is the voltage level of the DC bus.

Moreover, L_{Tx}, C_{Tx} and R_{Tx} (x = 1, 2) denote the self-inductance, the compensation capacitor and the parasitic equivalent series resistance (ESR) of the given transmitter, respectively. $M_{Tx\text{-}R}$ represents the mutual inductance between each transmitter and the pickup coil, whereas $M_{T1\text{-}T2}$ refers to the mutual inductance between the neighboring transmitting coils. I_1, I_2 correspond to the primary and secondary side currents, ω is the angular resonance frequency, and j is the imaginary unit. It is important to emphasize that all compensation tanks operate under resonance; thus, the voltage drop across them is omitted, i.e., $j\omega L = 1/(j\omega C)$. Additionally, the winding ESRs are considered negligible to simplify the analysis.

First, regarding the SOM equivalent circuit, the SRPC output voltage V_{SRPC} is equal to jKI_1. By implementing the Kirchhoff's voltage law (KVL) to the primary and secondary sides, the following equations are attained:

$$\overrightarrow{I_1} = \frac{\overrightarrow{V_{rect}}}{j\omega M_{T1-R}} \tag{3}$$

$$\overrightarrow{V_{inv}} = jK\overrightarrow{I_1} - j\omega M_{T1-R}\overrightarrow{I_2}. \tag{4}$$

It should be noted that the charging current can be obtained from the FHA equivalent rectifier circuit as:

$$I_{out} = \frac{2\sqrt{2}\left|\overrightarrow{I_2}\right|}{\pi}. \tag{5}$$

In Fig. 3c, the SOM phasor diagram is illustrated. Considering a fully tuned secondary side, $\overrightarrow{V_{rect}}$, $\overrightarrow{I_2}$ are in phase, whilst $\overrightarrow{I_1}$, $\overrightarrow{I_2}$ are 90° apart[21]. The apostrophe indicates how the quantities are altered with the SRPC participating in the reactive power flow. The phase shift between $\overrightarrow{V_{inv}}$ and $\overrightarrow{I_1}$ can be deduced as:

$$\varphi = \sin^{-1}\frac{K\left|\overrightarrow{I_1}\right|}{\left|\overrightarrow{V_{inv}}\right|}. \tag{6}$$

Consequently, when K is set to zero, i.e., the SRPC is short-circuited, the two quantities are in phase (φ = 0°). In this case, the HFI transitions are hard-switched. In contrast, when K receives a positive value, ZVS conditions are achieved, since $\varphi \neq 0°$.

The expressions of the ISOM equivalent circuit are determined as:

$$\overrightarrow{I_1} = \frac{\overrightarrow{V_{rect}}}{j\omega M_{T1-R} + j\omega M_{T2-R}} = \frac{\overrightarrow{V_{rect}}}{j\omega M_{TOT}} \tag{7}$$

$$\begin{aligned}\overrightarrow{V_{inv}} &= 2j\omega M_{T1-T2}\overrightarrow{I_1} - jK\overrightarrow{I_1} - j\omega M_{T1-R}\overrightarrow{I_2} - j\omega M_{T2-R}\overrightarrow{I_2} = \\ &2j\omega M_{T1-T2}\overrightarrow{I_1} - jK\overrightarrow{I_1} - j\omega M_{TOT}\overrightarrow{I_2} \Rightarrow \overrightarrow{I_2} = \\ &\frac{j\left|\overrightarrow{Vinv}\right|\angle 0° + (2\omega M_{T1-T2} - K)\left|\overrightarrow{I_1}\right|\angle -\varphi}{\omega M_{TOT}}\end{aligned} \tag{8}$$

$$\varphi = \sin^{-1}\frac{2\omega M_{T1-T2}\left|\overrightarrow{I_1}\right| - K\left|\overrightarrow{I_1}\right|}{\left|\overrightarrow{V_{inv}}\right|}. \tag{9}$$

The studied phase angles refer to the vector of $\left|\overrightarrow{Vinv}\right|\angle 0°$. From Eq. (7), it becomes evident that the immoderate increase of the primary current is confined thanks to the coincidental energization of the adjacent transmitters and the consequent summation of the individual mutual inductances between each transmitting coil and the receiver. The effect of the cross coupling between the transmitters can be observed from Eqs (8) and (9). When the SRPC configuration is not integrated, φ is raised, i.e., the HFI output impedance is highly inductive. As a result, the secondary current, and by extension, the charging power are, drastically decreased. The SRPC offsets the term $2j\omega M_{T1-T2}$ and contributes to the reduction of φ and the boost of the receiver current, as can be seen in Fig. 3e.

AC switching subsystem

The ACS subsystem's purpose is the selective activation of the transmitting coils, aiming at the enhancement of the efficiency and the electromagnetic leakage characteristics of the dynamic wireless charger. In Fig. 4a, the ACS subsystem circuit diagram of the first two transmitters is displayed. Each resonant network (transmitter winding along with the in-series compensation capacitor) terminal is connected to a dual common source MOSFET module (S_{Tx}, S_x). Depending on the EV position, the charger has to either enter the SOM or the ISOM by turning on the appropriate switches. Hence, the switching sequence of Fig. 4b is acquired. In particular, when a new EV accesses the charger, S_{T1} and S_2 are activated, leading to the ISOM. This state is maintained briefly to prevent the emergence of overcurrent in the primary circuit. The increase of $M_{T1\text{-}R}$ marks the

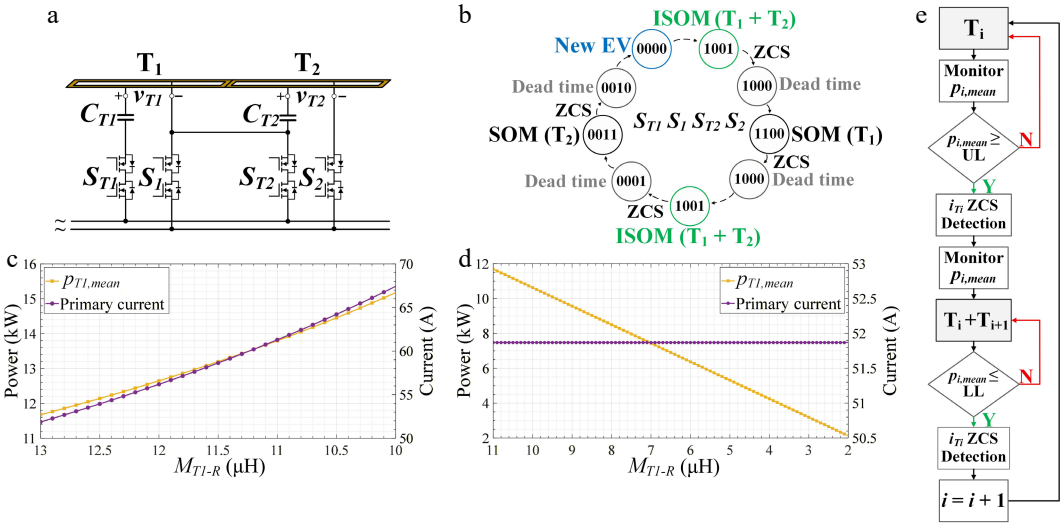


Fig. 4 ACS subsystem. (a) Circuit diagram. (b) Switching states sequence. (c) Transmitter current and active power vs $M_{Tx\text{-}R}$ (SOM to ISOM). (d) Transmitter current and active power vs $M_{Tx\text{-}R}$ (ISOM to SOM). (e) Control strategy flowchart.

shift to the SOM and the energization of T_1. To avoid the repercussions caused by the *di/dt* transients, the ACS controller realizes the deactivation of S_2 only when the transmitter current zero-crossing occurs, whilst introducing the necessary dead time. S_1 subsequently, is turned on without any current flowing through the circuit. Thereby, the incurred switching losses are significantly reduced, and no overvoltage manifests across the transmitting coils. As the EV moves towards the succeeding transmitter, ISOM is once again activated (S_1 turn-off, S_2 turn-on) under zero-current switching (ZCS) conditions. The $M_{T1\text{-}R}$ decrease entails the sole energization of T_2 (S_{T1} turn-off and S_{T2} turn-on). Next, ISOM is applied with the in-series connection of T_2 and T_3, whilst the subsequent $M_{T2\text{-}R}$ mitigation leads to the exclusive activation of T_3. The same procedure is employed for the rest of the transmitting windings.

Since the actuation of each coil is premised on the EV position, a detection system is required. To abstain from the utilization of complex techniques, which deploy real-time communication protocols of extremely low latency and enhanced range, the ACS controller leverages the impact the EV movement has on the mutual inductance. Specifically, the real power mean value of each transmitter, i.e., the active power, is monitored. By measuring the voltage across the coil (v_{Tx}), as well as the primary current, and by assuming that its phase shift relative to the secondary current is 90°, the amplitude of the active power is obtained:

$$P_{Tx,mean} = -j\omega M_{Tx-R}\left|\vec{I_2}\right|\left|\vec{I_1}\right|\sin\varphi_{I_1-I_2} \Rightarrow \left|P_{Tx,mean}\right| = \omega M_{Tx-R}\left|\vec{I_2}\right|\left|\vec{I_1}\right| \quad (10)$$

Fig. 4c showcases how $P_{Tx,mean}$ varies during the transition from the SOM to ISOM. The $M_{Tx\text{-}R}$ decrease results in a decrease in transmitter current, and, therefore, the active power rise. When $P_{Tx,mean}$ surpasses a pre-defined upper limit (UL), ISOM is activated, as demonstrated in Fig. 4e. As can be seen in Fig. 4d, the further reduction of $M_{Tx\text{-}R}$, while the EV approaches the following winding, induces the descent of $P_{Tx,mean}$. The switchover to the succeeding transmitter (SOM) is carried out at the moment when $P_{Tx,mean}$ falls below a determined low limit (LL). It should be highlighted that during the transition from one transmitter group, supplied by one HFI, SRPC pair, to the next (e.g., when the EV moves from T_{x10} to T_{x11}), the increase in $P_{Tx,mean}$ signifies the actuation of the interlock mechanism, meaning that the subsequent ISOM is fed by the following converter module.

Simulation results

A MATLAB/Simulink and PLECS co-simulation model is deployed for the verification of the proposed DWC system's smooth operation. The power circuit is realized in the PLECS software environment, whereas the SRPC and ACS control strategies, as well as the code employed for the variation of the magnetic coupler parameters, are developed in MATLAB/Simulink. In more detail, the pulse sequences generated by the control schemes are inserted in the PLECS environment, which, in turn, outputs the measured power circuit quantities needed for the control implementation. Both models run at the same time step (11.76 ns). Concurrently, a lookup table that contains the mutual and self-inductances of the couplers (as presented in Fig. 2h, i) is accessed by the developed MATLAB script, and its values are introduced in PLECS. The code is executed at a slower rate (0.005 s), emulating the EV speed (36 km/h), while it travels along the transmitting array.

The foremost simulation study parameters are listed in Table 1. A typical EV battery voltage level is employed, whilst the compensation capacitance values are derived from the resonance frequency expression. Since the self-inductances do not really fluctuate during the EV movement (Fig. 2h), mean values are considered for the transmitter and receiver compensation capacitance calculations (52 μH for the former and 106 μH for the latter). Furthermore, a current transformer of 1:1 turns ratio is utilized for the interconnection of the SRPC to the AC bus to prevent the short-circuiting of the common DC bus.

Steady-state results

Initially, steady-state results, which substantiate the SRPC usefulness, are obtained. In Fig. 5a–d, SOM waveforms with the SRPC topology incorporated in the primary side and without it are presented. The mutual inductance between the transmitter and the receiver is set to 13 μH. The integrated configuration acts as a virtual inductor, and thus, the primary current lags the SRPC output

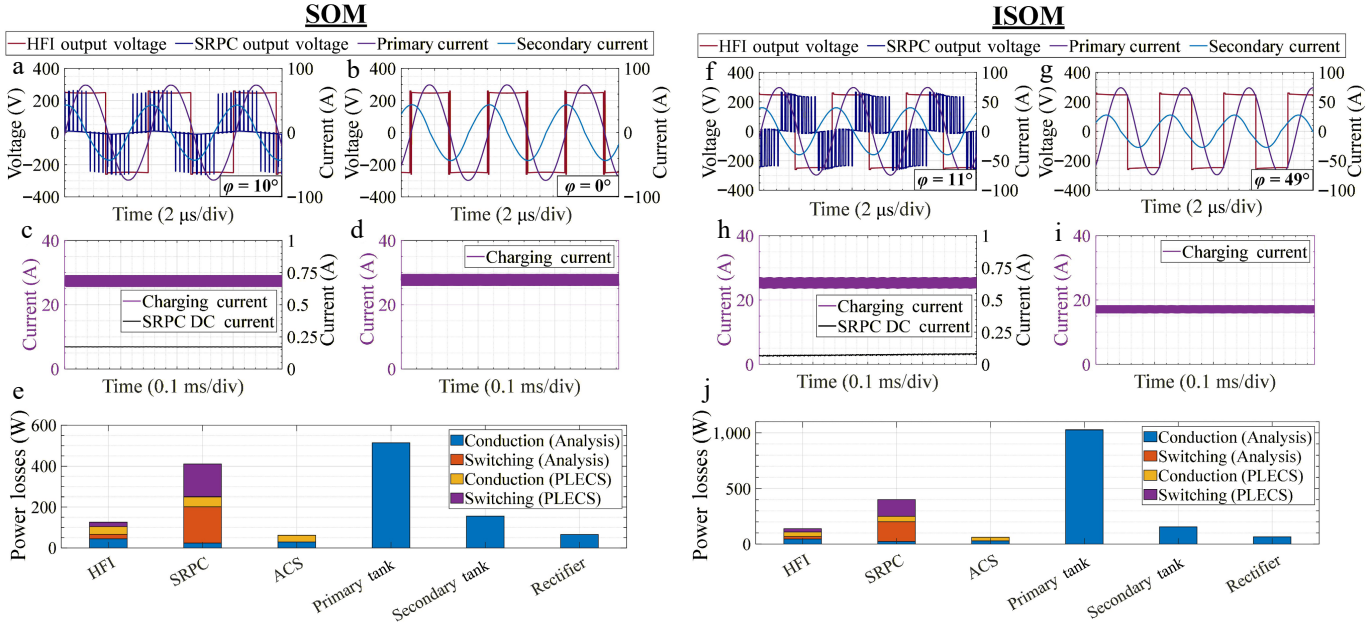


Fig. 5 Steady-state simulation results. (a)–(d) SOM waveforms. (e) SOM power loss analysis. (f)–(i) ISOM waveforms. (j) ISOM power loss analysis.

https://doi.org/10.48130/wpt-0026-0023

voltage by 90° (Fig. 5a). This results in the increase of the phase shift between the HFI output voltage and current waveforms from 0 to 10°. Hence, the HFI ZVS conditions are acquired without the deterioration of the DWC system power transfer capabilities, as evident from Fig. 5c, d The SRPC DC current, and by extension the active power processed by the topology, are substantially confined. On the other hand, in ISOM, the SRPC becomes a virtual capacitor. $M_{T1\text{-}R}$ and $M_{T2\text{-}R}$ are both tuned to 6.5 μH. The phase delay between the HFI output voltage and current is mitigated from 49° to 11°, as can be observed in Fig. 5f, g. The cross-coupling between the two transmitters is effectively attenuated, and therefore, the power delivered to the EV is greatly enhanced, reaching the nominal value of 11.2 kW (the divergence from the mathematical analysis nominal power value, i.e., 11.5 kW, is attributed to the presence of the transmitter and power switches' ESRs) as opposed to 6.8 kW (Fig. 5h, i).

What is more, in order to assess the proposed DWC system efficiency and to showcase its feasibility under real application conditions, an evaluation of its power losses in both operation modes is conducted. The average power losses over a current cycle are calculated, whilst a thermal study is performed on PLECS, since its thorough loss-estimation approach guarantees reliable results regarding the dissipation of the main converters and the ACS subsystem[22]. Table 1 contains the compensation capacitances and the semiconductor devices that were utilized. The voltage and current ratings of each recommended component meet the requirements of the full-scale application. For the HFI and ACS subsystem, MOSFET-based devices are selected, whereas the high operating frequency of the SRPC calls for GaN-based switches. Their specifications are obtained from the manufacturer datasheets. With respect to the HFI, the turn-on losses and the heat dissipation due to the charging and discharging of the parasitic output capacitor (C_{oss}) are both distinctly abated in the SOM and the ISOM, as the inverter operates in the inductive region, and thus, the ZVS transitions are achieved. Consequently, the turn-off, as well as the losses that incurred thanks to the antiparallel diode reverse recovery process, are the main switching loss mechanisms. They are determined as in Di et al.[23].

$$P_{turn-off,HFI} = V_{DC} \cdot I_{1,peak} \cdot sin\varphi \cdot t_{f,HFI} \cdot f_{sw,HFI} \tag{11}$$

$$P_{rev,HFI} = Q_{rr,HFI} \cdot V_{SD,HFI} \cdot f_{sw,HFI} \tag{12}$$

$$P_{sw,HFI} = 2 \cdot (P_{turn-off,HFI} + P_{rev,HFI}) \tag{13}$$

where $I_{1,peak}$ is the peak primary current, $t_{f,HFI}$ stands for the fall time, Qrr, HFI the recovered charge and $V_{SD,HFI}$ the reverse voltage drop of the selected SiC MOSFET. The HFI conduction losses, attributed to the drain-source on resistance ($R_{DS,on,HFI}$) and the forward voltage drop of the body diode during the dead time ($t_{deadtime,HFI}$) introduced to avoid shoot-throughs, are deduced as[23];

$$P_{cond,HFI,active} = {I_{1,rms}}^2 \cdot R_{DS,on,HFI} \tag{14}$$

$$P_{cond,HFI,deadtime} = 2 \cdot t_{deadtime,HFI} \cdot f_{sw,HFI} \cdot [V_{body\ diode,HFI} \cdot I_{1,peak} \cdot sin\varphi + (I_{1,peak} \cdot sin\varphi)^2 \cdot R_{body\ diode,HFI}] \tag{15}$$

$$P_{cond,HFI} = 2 \cdot (P_{cond,HFI,active} + P_{cond,HFI,deadtime}). \tag{16}$$

where $V_{body\ diode,HFI}$ and $R_{body\ diode,HFI}$ stand for body diode voltage drop and dynamic resistance, accordingly. Additionally, the V/I overlap and the C_{oss} related losses constitute the main heat dissipation sources during the SRPC switching transients, since the GaN-based devices feature zero reverse recovery charge. For the preservation of the switches' temperature within an acceptable range, each one of them is composed of four GaN HEMTs. They are computed by Zou et al. as follows[24]:

$$P_{turn-on,SRPC} = E_{on} \cdot \frac{f_{sw,SRPC}}{\pi} \cdot \frac{V_{DC} \cdot I_{1,peak}}{n_{SRPC} \cdot V_n \cdot I_n} \tag{17}$$

$$P_{turn-off,SRPC} = E_{off} \cdot \frac{f_{sw,SRPC}}{\pi} \cdot \frac{V_{DC} \cdot I_{1,peak}}{n_{SRPC} \cdot V_n \cdot I_n} \tag{18}$$

$$P_{oss,SRPC} = {V_{DC}}^2 \cdot C_{oss,SRPC} \cdot f_{sw,SRPC} \tag{19}$$

$$P_{sw,SRPC} = 4 \cdot n_{SRPC} \cdot \left(P_{turn-on,SRPC} + P_{turn-off,SRPC} + P_{oss,SRPC}\right) \tag{20}$$

where E_{on} and E_{off} represent the turn-on and turn-off energy losses under the rated voltage (V_n) and current (I_n) test conditions, respectively, whilst n_{SRPC} denotes the number of parallel-connected GaN switches. Notably, the conduction losses of one SRPC leg ($P_{cond,SRPC,active}$) are independent of the USPWM modulation index or the phase difference between the output voltage and current[23]. The dead time loss ($P_{cond,SRPC,deadtime}$) and the conduction time decrease by the dead time duration ($P_{cond,SRPC,red}$) are also accounted for by Zou et al[24].

$$P_{cond,SRPC,active} = \frac{{I_{1,p}}^2 \cdot R_{DS,on,HFI}}{4 \cdot {n_{SRPC}}^2} \tag{21}$$

$$P_{cond,SRPC,deadtime} = \frac{t_{deadtime,SRPC} \cdot f_{sw,SRPC}}{\pi} \cdot \cdot \left(\frac{\pi}{2} \cdot R_{SD,SRPC} \cdot \frac{{I_{1,p}}^2}{{n_{SRPC}}^2} + 2 \cdot V_{SD,SRPC} \cdot \frac{I_{1,p}}{n_{SRPC}}\right) \tag{22}$$

$$P_{cond,SRPC,red} = \frac{{I_{1,p}}^2}{2 \cdot {n_{SRPC}}^2} \cdot (R_{DS\,on,SRPC} \cdot t_{deadtime,SRPC} \cdot f_{sw,SRPC}) \tag{23}$$

$$P_{cond,SRPC} = 2 \cdot n_{SRPC} \cdot (P_{cond,SRPC,active} + P_{cond,SRPC,deadtime} - P_{cond,SRPC,red}). \tag{24}$$

Moreover, the ACS subsystem transitions occur sporadically (depending on the EV speed), under ZCS conditions, whilst the rectifier consists of Schottky diodes with zero reverse-recovery charge; thus, the incurred loss in both cases is negligible. Their conduction losses along with those of the resonant tanks can be expressed according to Gonzalez-Gonzalez et al. as[25]:

$$P_{cond,ACS} = 2 \cdot {I_{1,rms}}^2 \cdot R_{DS,on,ACS} \tag{25}$$

$$P_{cond,Rect} = 2 \cdot \left(R_{F,Rect} \cdot {I_{2,rms}}^2 + V_{F,Rect} \cdot I_{2,rms}\right) \tag{26}$$

$$P_{primary\ tank} = {I_{1,rms}}^2 \cdot (R_T + R_{C1}) \tag{27}$$

$$P_{secondary\ tank} = {I_{2,rms}}^2 \cdot (R_R + R_{C2}) \tag{28}$$

where $R_{DS,on,ACS}$ is the on-resistance of each ACS switch (two devices are connected to each resonant tank), $R_{F,Rect}$ is the dynamic resistance and $V_{F,Rect}$ the voltage drop of the rectifier diodes, R_T, R_R stand for the ESRs of the transmitter and receiver windings, whilst R_{Cx} is the ESR of the compensation capacitors.

In Fig. 5e, j, the obtained SOM and ISOM results are depicted, respectively. The congruity between the power loss analysis and the thermal models provided by the given manufacturers becomes apparent. The most notable divergence can be observed in the case of the SRPC conduction losses; nevertheless, it can be ascribed to the raised switch temperature of the thermal study and the corresponding variation of the $R_{DS,on,SRPC}$ value. Evidently, the primary resonant tank conduction loss, which results from the 0.155-Ω transmitter winding and 0.028-Ω compensation capacitor, is what truly deteriorates the system efficiency. Its effect becomes even more prominent in the ISOM case, when two windings are connected in series. Particularly, by using the HFI, SPRC and ACS power losses derived from PLECS and the analysis calculations for the remaining DWC system components, a 5% drop is recorded, as the efficiency

falls from 91.23% (in the SOM) to 86.7% (in the ISOM). However, this reduction is permitted for the suppression of the charging power fluctuations.

Dynamic results

Next, the EV movement across neighboring transmitting coils is simulated. To avoid excessive simulation run times, only a few of the inductance lookup table values are accessed; specifically, the ones near the EV transition region, as depicted in Fig. 6h. In Fig. 6a, the HFI and SRPC output voltage and the primary current waveforms are displayed, whilst in Fig. 6e, f, the ACS subsystem pulses along with the transmitting coil active power are illustrated. Firstly, the DWC system operates in SOM, since the mutual inductance between the first transmitter and the receiver is higher than 11 μH (at the time instant t_1). From Fig. 6b, it is apparent that the SRPC configuration successfully imposes the HFI ZVS conditions. Subsequently, the $M_{T1\text{-}R}$ decrease results in the raising of the transmitted power (Fig. 6e, at the time instant t_2), and hence, the ACS subsystem controller immediately activates ISOM by turning off S_1 and turning on S_2. The wireless charger stays in that state until the time instant t_6, while the SRPC 'generates' reactive power (Fig. 6c). Apparently, the HFI operation in the inductive region, and consequently, the soft-switching transitions are maintained. The further reduction of the mutual inductance between the first transmitter and the pickup coil leads to the slight drop of the transferred power below the defined low limit and the energization of the succeeding winding (Fig. 6d).

In Fig. 6g, the charging and SRPC DC currents are presented. The latter is markedly limited, as the maximum value hardly reaches 0.35 A. The mean value of the former is equal to 28 A in the SOM. When the charger enters the ISOM, it falls to 23 A (at instant t_2), and it gradually returns to 27.6 A (at the time instant t_5), as the vehicle advances. The SRPC does, indeed, counteract the cross-coupling effect, since the charging current does not decline severely. However, the varying value of the mutual inductance between the adjacent transmitters (Fig. 6h) and the fixed control gain K preempt the even compensation. The nullification of $M_{T1\text{-}T2}$ is not sought-after, as it would lead to the loss of the inverter ZVS mode. It should be underlined that the Δi of 4.5 A corresponds to a 16 % transferred power drop. Nonetheless, the deviation from the nominal charging current lasts for just 20 ms; an insignificant span compared to the time spent in the SOM (115 ms). In parallel, the charging current can diverge from 28 A due to the lateral displacement tolerance feature, as evident in Fig. 6g (at the time instant t_6 and onward). A Δi of 3 A, or equivalently a 7.1% charging power decrease, is recorded, since $M_{T2\text{-}R}$ is raised from 11 to 13 μH (at the time instant t_7). Nevertheless, the intense power fluctuations observed in segmented-based coupler topologies, where the transmitters are fully deenergized during the transition between abutting windings, are absent, in all respects.

In addition, the entrance of a new EV into the DWC system is simulated. In order to charge the compensation capacitors up to the voltage level, they would reach during the accommodation of a previous EV, the test begins in ISOM, since the charger operates in this mode, when the vehicle moves aways from each resonant tank (Fig. 7h). In Fig. 7a, the HFI output voltage, the primary current and the compensation capacitor voltages in per unit (p.u.) system (i.e., $V_{inv,base}$ = 250 V, $I_{1,base}$ = 100 A, $V_{c,base}$ = 3,500 V) are displayed. At the time instant t_2, the charger enters an idle state, i.e., every ACS subsystem switch is turned off (Fig. 7f, g). As can be seen in Fig. 7b, the devices are deactivated under ZCS conditions, while the current slope is negative. During this moment, the voltage across each compensation capacitor crosses the positive peak value and remains at that level with the ACS devices deactivated (thanks to the 90° phase shift between the capacitor voltage and current waveforms). As a new EV accesses the charger (at the time instant t_3), the switchover to ISOM occurs only when the HFI output voltage falls from $+V_{DC}$ to $-V_{DC}$. Thereby, the excessive rise of the capacitor voltage is prevented (Fig. 7c). This practice is applied for every AC switch turn-off. In Fig. 7d, the ISOM waveforms are depicted, highlighting the equal voltage distribution between the two capacitors, whereas in Fig. 7e, the SOM quantities are illustrated. Lastly, it should be noted that a distance sensor, which detects the EV approaching the charger and triggers the HFI pulse generation, is assumed ($t_2 < t < t_3$).

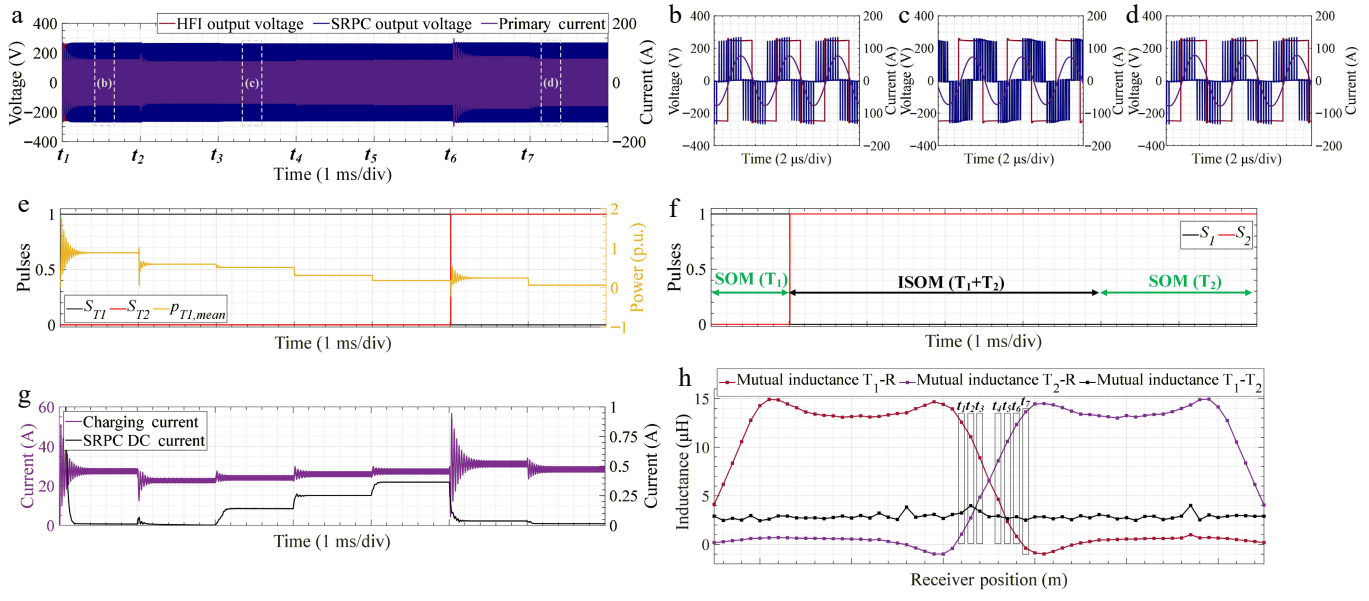


Fig. 6 Simulation results for the EV transition across adjacent transmitting coils. (a)–(d) HFI, SRPC output voltage and primary current waveforms. (e) ACS subsystem pulses and transferred active power. (f) ACS subsystem pulses. (g) Charging current and SRPC DC current. (h) Mutual inductance values vs pickup coil position.

https://doi.org/10.48130/wpt-0026-0023

Discussion

In all, the proposed DWC system constitutes a moderate solution that takes into account the minimization of the capital investment cost, ensures the satisfactory and continuous power transfer to the EV even under displaced conditions, as well as, the selective activation of the transmitting coils based on the receiver position. Thereby, the incurred energy waste is mitigated, whilst the overall system efficiency is improved. A comparison analysis between the proposed and other DWC systems in the literature can be summarized as follows (additional details are provided in Table 2):

1) The total length of litz wire needed for the construction of a 1 km long charging lane is equal to 16 km. None of the prior art, except for[9,10], features such low laying demands.

2) Two inverters and 1,334 power switches are requisite for the 1 km long lane installation. More power electronic devices are needed for the systems included in[2–6,14,17].

3) A total of 667 compensation capacitors are necessary for the proposed dynamic charger. Most systems require an increased count of primary passive elements (inductors/capacitors)[1–8,12–14,17].

4) The maximum output power fluctuation does not surpass 16% of the nominal charging power under fully-aligned and laterally misaligned conditions (±6 cm). This does not stand for the works presented in[5–9,14]. In fact, most of them do not account for any lateral displacement[1–8,12,14].

5) A compact receiver design is realized, as it is equipped with solely one 500 × 500 mm winding and a passive rectifier, unlike the works in[3,6,7,9–11,14].

6) A selective transmitter excitation and an EV detection method without an established real-time communication link are incorporated. Although necessary, the former is not considered in[1,3,5,12,13], whereas the latter is absent from most systems[1–3,5–7,12,13,17].

7) Soft-switching conditions are achieved for the HFI power devices, contrary to the other works[3,4,6,9,10,17].

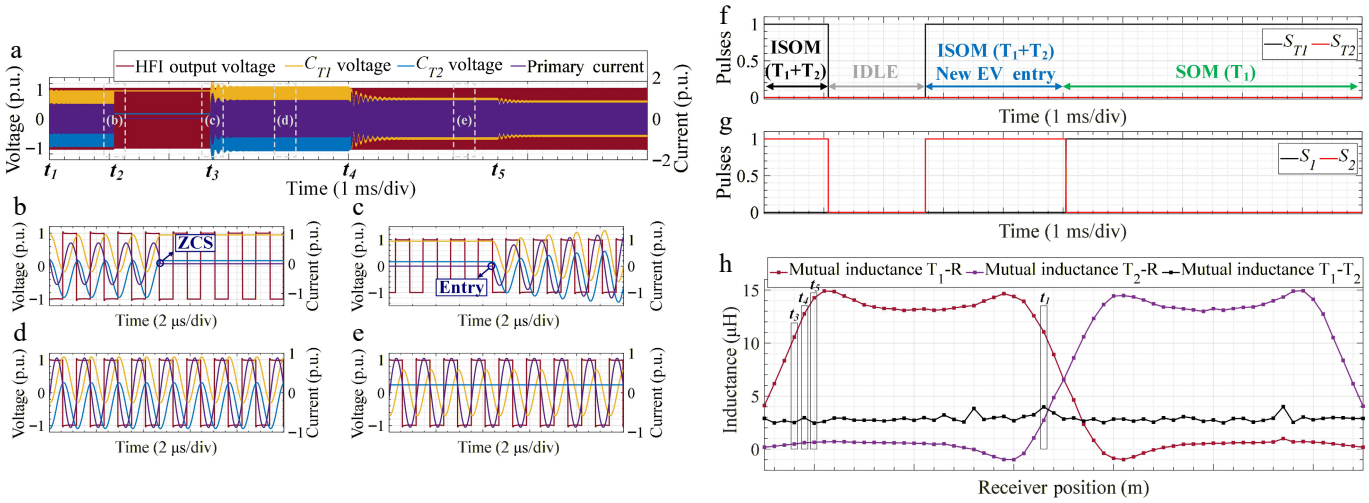


Fig. 7 Simulation results for the entrance of a new EV. (a)–(e) HFI output voltage, primary current, and compensation capacitor voltage waveforms. (f), (g) ACS subsystem pulses. (h) Mutual inductance values vs pickup coil position.

Table 2. Comparison with related work.

	C_{TOTAL} (km)	Comp. elements (km)	Power devices (km)	Selective coil activation	Receiver size (mm)	Output power fluctuation	Lateral misalign	EV detection system
[1]	35 (+ comp. inductor wire)	7,500	One inverter	×	485 × 400	7.5%	×	×
[2]	70 (+ comp. inductor wire)	15,000	One inverter + 5,000 switches	√	400 × 200	2%	×	×
[3]	31.2	2,000	2,000 Inverters	×	600 × 300	3.5%	×	×
[4]	94.24	11,538	3,846 Inverters + 3,846 switches	√	130 × 130	4.8%	×	√ (wireless comm. required)
[5]	–	20,001	6,667 switches	×	150 × 150	76.85%	×	×
[6]	39.9 (main coils) + 13.275 (coupled connector)	5,000	417 inverters + 1,250 switches	√	700 × 630	33%	×	×
[7]	–	2,084	1,043 switches	√	760 × 500	100%	×	×
[8]	93.12	8,696 + 2	One inverter	√	230 × 130	100%	×	Not required
[9]	10.23	1	One inverter	Not required	1,200 × 600	36.7%	√	Not required
[10]	7.34	1	One inverter	Not required	3,150 × 900	14.6%	√	Not required
[11]	20.4	9	One inverter (three-phase)	Not required	600 × 600	5.6%	√	Not required
[12]	22.85	4,304	One inverter	×	400 × 400	4%	×	×
[13]	35.77	3,228	One inverter	×	400 × 400	6%	√	×
[14]	–	1,000	1,000 inverters	√	1,000 × 600	100%	×	√
[17]	46.72	2,000 + 3	One inverter + 4,000 switches	√	150 × 150	2%	√	√ (wireless comm. required)
This work	16	667	Two inverters + 1,334 switches	√	500 × 500	16%	√	√

√: considered/included, ×: not considered/included, –: means not given.

Conclusions

In this article, a soft-switched EV dynamic wireless charger of extremely low laying requirements has been proposed. A selective activation system for its couplers, which alleviates the need for a real-time communication link, is integrated, whilst the excessive utilization of semiconductor devices is avoided. The design process and mathematical analysis of each subsystem are explicitly explained. A thorough MATLAB/Simulink and PLECS co-simulation study using data derived from ANSYS MAXWELL verifies the efficacy and overall good performance of the proposed DWC system.

Author contributions

The authors confirm their contributions to the paper as follows: study conception and design: Dimitriadou K, Albanopoulos I, Papanikolaou N, Yang Y; data collection: Dimitriadou K, Albanopoulos I; analysis and interpretation of results: Dimitriadou K, Albanopoulos I, Papanikolaou N, Yang Y; draft manuscript preparation: Dimitriadou K, Albanopoulos I, Papanikolaou N, Yang Y. All authors reviewed the results and approved the final version of the manuscript.

Data availability

The data that support the findings of this study are available on request from the corresponding author, Papanikolaou N.

Acknowledgments

No funding was received for this work.

Conflict of interest

The authors declare that they have no conflict of interest.

Dates

Received 24 March 2026; Revised 1 June 2026; Accepted 24 June 2026; Published online 30 October 2026

References

[1] Lu F, Zhang H, Hofmann H, Mi CC. 2016. A dynamic charging system with reduced output power pulsation for electric vehicles. *IEEE Transactions on Industrial Electronics* 63(10):6580–6590

[2] Li Y, Hu J, Lin T, Li X, Chen F, et al. 2019. A new coil structure and its optimization design with constant output voltage and constant output current for electric vehicle dynamic wireless charging. *IEEE Transactions on Industrial Informatics* 15(9):5244–5256

[3] Zhang Y, Zhou H, Shen Z, Xie R, Chen Z, et al. 2024. An interoperable dynamic wireless charging system with stable output based on a self-adaptive two-pole receiver. *IEEE Transactions on Power Electronics* 39(10):11943–11947

[4] Xiong W, Tan J, Liu Z, Zhu Q, Sun Y, et al. 2025. A repeater-based dynamic wireless power transfer system with controllable detuning rate for a constant output profile. *IEEE Transactions on Power Electronics* 40(7):10176–10188

[5] Wang R, Wang Y, Ding P, He Y, Ma Z, et al. 2026. Design and implementation of a high-frequency inverter with wide soft-switching range for dynamic wireless charging of electric vehicles. *Wireless Power Transfer* 13:e003

[6] Barsari VZ, Thrimawithana DJ, Kim S, Covic GA. 2023. Modular coupler with integrated planar transformer for wireless EV charging. *IEEE Transactions on Power Electronics* 38(7):9206–9217

[7] Barsari VZ, Thrimawithana DJ, Covic GA. 2021. An inductive coupler array for in-motion wireless charging of electric vehicles. *IEEE Transactions on Power Electronics* 36(9):9854–9863

[8] Jeong SY, Park JH, Hong GP, Rim CT. 2019. Autotuning control system by variation of self-inductance for dynamic wireless EV charging with small air gap. *IEEE Transactions on Power Electronics* 34(6):5165–5174

[9] Song B, Dong S, Li Y, Cui S. 2020. A dual-layer receiver with a low aspect ratio and a reduced output fluctuation for EV dynamic wireless charging. *IEEE Transactions on Power Electronics* 35(10):10338–10351

[10] Cui S, Wang Z, Han S, Zhu C, Chan CC. 2019. Analysis and design of multiphase receiver with reduction of output fluctuation for EV dynamic wireless charging system. *IEEE Transactions on Power Electronics* 34(5):4112–4124

[11] Vu VB, Dahidah M, Pickert V, Phan VT. 2020. A high-power multiphase wireless dynamic charging system with low output power pulsation for electric vehicles. *IEEE Journal of Emerging and Selected Topics in Power Electronics.* 8(4):3592–3608

[12] Shi K, Tang C, Wang Z, Li X, Zhou Y, et al. 2022. A magnetic integrated method suppressing power fluctuation for EV dynamic wireless charging system. *IEEE Transactions on Power Electronics* 37(6):7493–7503

[13] Shi K, Tang C, Feng T, Wang P, Jiang J, et al. 2025. Novel integrated optimization to enhance output stability and power capability in EV dynamic wireless charging under lateral misalignment. *IEEE Transactions on Power Electronics* 40(10):15959–15975

[14] Meira Gomes Z, de Oliveira Prado E, Le Gall Y, Damm G, Ripoll C, et al. 2025. Design, model, and control of a dynamic wireless power transfer system for a 30-kW electric vehicle charger application. *IEEE Journal of Emerging and Selected Topics in Power Electronics* 13(3):3882–3894

[15] Wang H, Pratik U, Jovicic A, Hasan N, Pantic Z. 2021. Dynamic wireless charging of medium power and speed electric vehicles. *IEEE Transactions on Vehicular Technology* 70(12):12552–12566

[16] Karakitsios I, Palaiogiannis F, Markou A, Hatziargyriou ND. 2018. Optimizing the energy transfer, with a high system efficiency in dynamic inductive charging of EVs. *IEEE Transactions on Vehicular Technology* 67(6):4728–4742

[17] Cai C, Saeedifard M, Wang J, Zhang P, Zhao J, et al. 2022. A cost-effective segmented dynamic wireless charging system with stable efficiency and output power. *IEEE Transactions Power Electronics* 37(7):8682–8700

[18] Tan L, Zhao W, Liu H, Li J, Huang X. 2020. Design and optimization of ground-side power transmitting coil parameters for EV dynamic wireless charging system. *IEEE Access* 8:74595–74604

[19] Ibrahim M, Pichon L, Bwrnard L, Razek A, Houivet J, et al. 2015. Advanced modeling of a 2-kW series–series resonating inductive charger for real electric vehicle. *IEEE Transactions on Vehicular Technology* 64(2):421–430

[20] Akagi H, Watanabe EH, Aredes M. 2017. The instantaneous power theory. In *Instantaneous Power Theory and Applications to Power Conditioning. 2nd ed*. Hoboken, NJ: Wiley-IEEE Press. pp. 37–109 doi: 10.1002/9781119307181

[21] Feng H, Cai T, Duan S, Zhang X, Hu H, et al. 2018. A dual-side-detuned series–series compensated resonant converter for wide charging region in a wireless power transfer system. *IEEE Transactions on Industrial Electronics* 65(3):2177–2188

[22] Batarseh MG, Samer Al-Jizawi Y, El-Faouri FS, Nidal Bulbul L. 2025. A novel unipolar pulse-width modulation scheme for single-phase H-bridge inverters with balanced switch loss distribution. *IEEE Access* 13:163235–163245

[23] Di Capua G, Femia N, Lisi G. 2016. Impact of losses and mismatches on power and efficiency of Wireless Power Transfer Systems with controlled secondary-side rectifier. *Integration* 55:384–392

[24] Zou M, Sun P, Zeng Z, Wang Y, Gong J, et al. 2025. Systematic efficiency-density co-optimization of 100 kW GaN traction inverter: methodology and integration. *IEEE Transactions on Power Electronics* 40(11):16281–16299

[25] Gonzalez-Gonzalez JM, Trivino-Cabrera A, Aguado JA. 2022. Assessment of the power losses in a SAE J2954-compliant wireless charger. *IEEE Access* 10:54474–54483

Copyright: © 2026 by the author(s). Published by Maximum Academic Press, Fayetteville, GA. This article is an open access article distributed under Creative Commons Attribution License (CC BY 4.0), visit https://creativecommons.org/licenses/by/4.0/.